# Supporting Information

# Confocal Fluorescence Microscopy of the Morphology and Composition of Interstitial Fluids in Freezing Electrolyte Solutions

Jie Cheng, Cherrie Soetjipto, Michael R. Hoffmann and A. J. Colussi*

*W. M. Keck Laboratories, California Institute of Technology, Pasadena, California 91125*

**jz-2009-000888-R2**

Phone: 01-626-395-4402; Fax: 01-626-395-2940; E-mail: ajcoluss@caltech.edu

**Experimental:** C-SNARF-1 (Invitrogen, C1270, see Scheme 1) was used as the dual-emission fluorescence pH indicator.[1] A 50 μM stock C-SNARF-1 solution in purified water was prepared and stored frozen at -20 ˚C until use. Sodium chloride (> 99.9% purity; EMD), ammonium acetate (> 99.999% purity; Aldrich), and ammonium sulfate (> 99.5% purity; EMD) were used as received. 1 M sodium hydroxide solution (VWR), 30% ammonium hydroxide solution (J.T. Baker), 1 M hydrochloric acid (VWR), 1 M sulfuric acid (VWR), $KH_2PO_4 \cdot 3H_2O$(AR; Mallinckrodt), and $KH_2PO_4$ (>99.7% purity; Mallinckrodt) were used to adjust the pH of the sample solutions as indicated. All solutions were prepared with deionized, ultrapure water (resistivity 18.2 MΩ cm) from a Millipore purification system.

Temporally- and spectrally-resolved fluorescence imaging of test solutions was performed with a Zeiss LSM 510 META NLO confocal laser scanning microscope (CLSM) equipped with a temperature-programmable PE-120 Peltier cryostage (Linkam). Air-equilibrated, [C-SNARF-1] = 1.0 μM test solutions were prepared by dilution of the stock solution in purified water, or in binary electrolyte solutions of known concentration, as indicated. Their pH was adjusted prior to freezing by addition of acid (base) sharing the same anion (cation) as the selected electrolyte. Test solution samples (30 μL) were contained in a cylindrical receptacle (diameter = 6.0 mm; depth = 1.0 mm) bored into a clear silica plate tightly clamped to the cryostage lying on the (*x*, *y*)-movable plate of the CLSM. A typical freeze-and-thaw cycle involved a temperature program consisting of three consecutive steps: (1) cooling at -10 K $min^{-1}$ from 298 K to 268 K, (2) holding at 268 K for 5 minutes after completion of sample freezing, (3) warming at 10 K $min^{-1}$ to 298 K. The actual sample temperature was measured with a calibrated type-K thin wire thermocouple immersed in the sample (Fig. 1). The fluorescence emitted by the sample was continuously scanned during the freeze-thaw cycle. The advancing ice front could be tracked by

adjusting the (*x, y*)-coordinates of the stage relative to the optical axis. LD C-Apochromat 40×/1.1 W Corr M27 or EC Plan-Neofluar 10×/0.3 objective lenses were used to collect images from *x*-*y* planes with (512 × 512) pixels resolution, which correspond to (225 μm × 225 μm) and (900 μm × 900 μm) frames, respectively. The following instrumental parameters were used unless otherwise specified: $\lambda_{exc}$ = 488 nm at 50% argon laser output power, 15% transmission; scan speed = 1.0 frame $s^{-1}$; pinhole set at 750, corresponding to a z-slice of < 9.3 μm for the 40×/1.1 objective; detector gain = 720. The META detector and the Lambda acquisition mode were used to obtain fluorescence emission spectra from 565.1 nm to 650.7 nm with a step size of 10.7 nm. The images acquired were analyzed using Zeiss LSM Image Examiner software.

$R = I(\lambda_1)/I(\lambda_2)$, is the ratio of their corresponding fluorescence intensities. Figure 1 shows *R* vs. pH calibration curves obtained by fitting equation (ES1):

$$\mathrm{pH} = \mathrm{p}K_a + \beta \log\frac{R - R_{\min}}{R_{\max} - R} + \log\frac{I^a}{I^b} \qquad \text{(ES1)}$$

to CLSM *R*-measurements at various temperatures. p$K_a$ (C-SNARF-1) = 7.5, $R_{max}$ and $R_{min}$ are the maximum and minimum *R*-values, and $I(\lambda_2)^a/I(\lambda_2)^b$ is the ratio of $I(\lambda_2)$ in acid to that in base. Ratiometric measurements minimize uneven probe distribution, differences in sample thickness, photobleaching and self-quenching effects.[2-4] As long as fluorescence does not oversaturate the detector, calibration curves are insensitive to sample concentration and instrumental parameters such as excitation laser intensity and scan speed (Fig. S2). Temperature has a minor effect on *R* vs. pH calibration curves (~ 0.01 pH $K^{-1}$) between 268 K and 298 K.[5] Other factors, such as ionic strength variations are negligible under present conditions.[6]

**Appendix S1.** A thermodynamic analysis of intergrain gap size, δ, has been recently carried out. Consider pockets containing different concentrations of the rejected electrolyte in a frozen sample under thermal equilibrium at $T_s$. Layered ice/water/ice arrays have a positive Hamaker constant and will tend to collapse via short range (retarded) dispersive forces.[7-9] In the presence of electrolytes, however, ice surfaces are charged by selective ion adsorption[10] and will, hence, repel each other via long-range Coulomb forces. The solute also resists closing the gap between ice surfaces because that will entail the loss of configurational entropy (the colligative effect). The polarizable ion atmosphere, in turn, will screen Coulombic forces with Debye lengths $D \propto C^{-½}$. Since surface charge density is nearly independent of temperature whereas $C$ necessarily increases at lower temperatures, the resulting δ vs. $C$ dependence is not trivial.[11,12] At low $C$, equilibrium may be reached at finite δ's (Case A). However, if ion adsorption on ice surfaces were already saturated, their Coulombic repulsion will be shielded more efficiently by the intervening ion atmosphere at higher $C$'s. Above some threshold $C$, the gap may become so narrow that short-range dispersive attraction forces become dominant and trigger a discontinuous transition to $\delta = 0$ (Case B). At fixed $T_s$, but at still higher $C$'s, colligative bulk effects may ultimately override surface forces (Case C). Based on this analysis, we consider that our system has meet the conditions of Case A in the experiment of Fig. 3a, and Case C in the experiments of Figs. 4 in 1 mM NaCl. This analysis, however, does not account for the formation of < 1 μm diameter brine inclusions in the latter case.

We conjecture that the bright regions at the bottom of Figs. 3b, c are remnants of the dendrites produced by bifurcation of the planar ice front,[13] which became themselves unstable along their growth axis and spawn discrete pockets. The average spacing between dendrites λ ~

10 μm produced by an ice front moving at $v \sim 10$ μm $s^{-1}$ is within predictions based on $v$-$\lambda$ stability diagrams for freezing $H_2O$/NaCl solutions.[13]

---

**Figure S1.** Fluorescence emission image (225 μm × 225 μm) of an aqueous solution containing 5 μM C-SNARF-1 and 0.05 mM $CH_3COONH_4$: a) before freezing at 298 K, and b) during thawing after being frozen for 5 minutes. c) fluorescence intensity at 618 nm and the pH value based on the fluorescence emission integrated over regions of interest (ROIs) 1-6; ROIs 1-4 show the accumulation of C-SNARF-1 at the surface of bubbles trapped in ice/water.

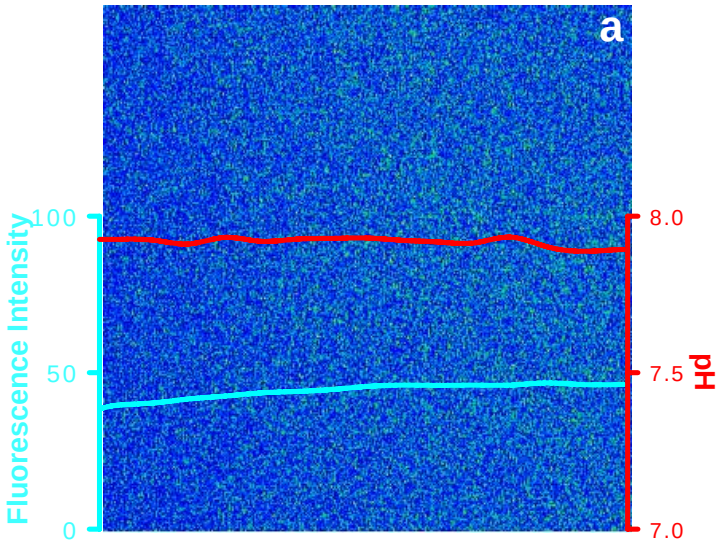

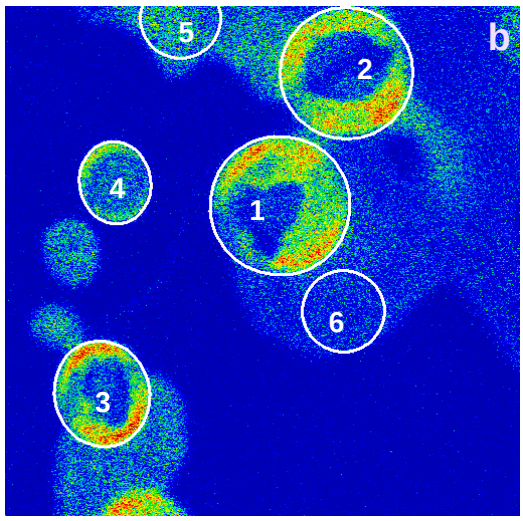
b
1
2
3
4
5
6

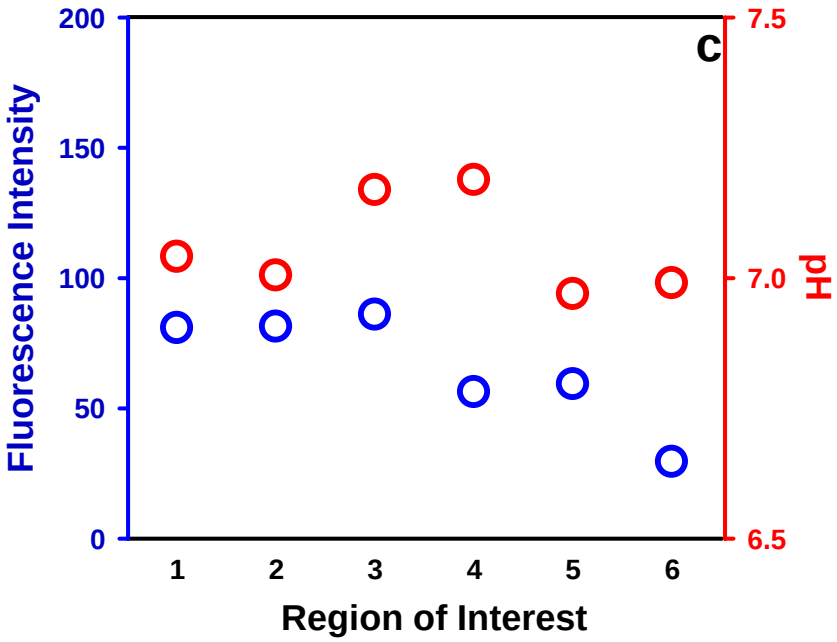
c
200
150
100
50
0
7.5
7.0
6.5
pH
Fluorescence Intensity
1
2
3
4
5
6
Region of Interest

**Figure S2**. Fluorescence emission spectra of C-SNARF-1 as a function of solution pH. [C-SNARF-1] = 1.0 μM, [$KH_2PO4$] + [$K_2HPO4$] = 0.05M, T = 298 K.

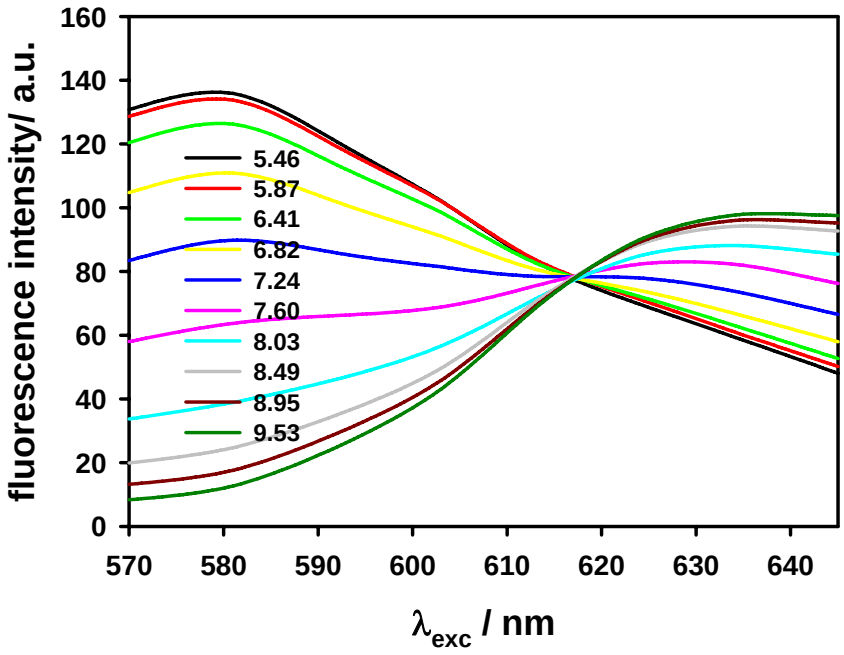

**Figure S3.** Fluorescence emission ratio of C-SNARF-1 versus (a) laser intensity in % of laser transmission and (b) [C-SNARF-1] in μM.

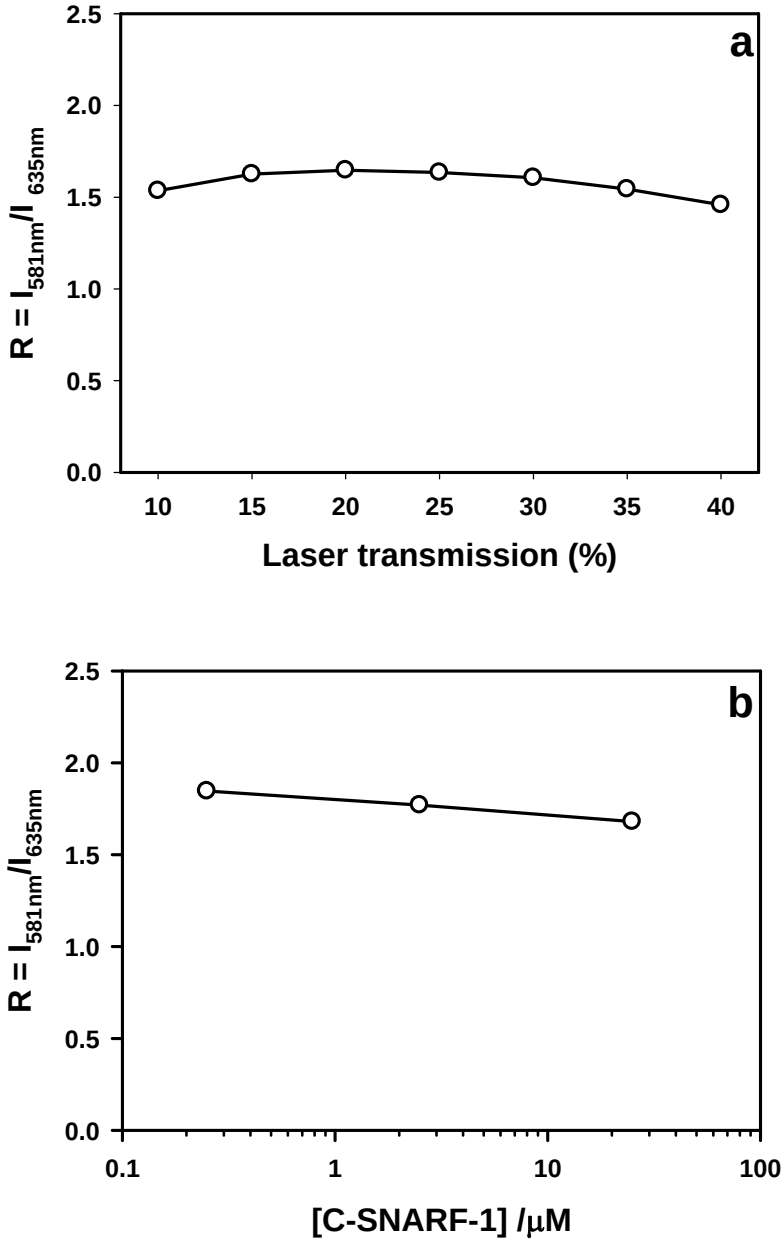

## References


1 Salerno, M.; Ajimo, J. J.; Dudley, J. A.; Binzel, K.; Urayama, P. Characterization of dual-wavelength seminaphthofluorescein and seminapthorhodafluor dyes for pH sensing under high hydrostatic pressures *Anal. Biochem.* **2007**, *362*, 258-267.

2 Pawley, J. B. *Handbook of biological confocal microscopy*, 2nd ed.; Plenum Press: New York, 1995.

3 Mason, W. T. *Fluorescent and luminescent probes for biological activity*, 2nd ed.; Academic Press: London, U.K., 1999.

4 Bassnett, S.; Reinisch, L.; Beebe, D. C. Intracellular ph measurement using single excitation-dual emission fluorescence ratios *Am. J. Physiol.* **1990**, *258*, C171-C178.

5 Taylor, M. J. The meaning of ph at low-temperatures *Cryo-Lett.* **1981**, *2*, 231-239.

6 Robinson, C.; Boxe, C. S.; Guzman, M. I.; Colussi, A. J.; Hoffmann, M. R. Acidity of frozen electrolyte solutions *J. Phys.l Chem. B* **2006**, *110*, 7613-7616.

7 Israelachvili, J. *Intermolecular and Surface Forces*; Academic Press: San Diego, CA, 1992.

8 Dash, J. G.; Rempel, A. W.; Wettlaufer, J. S. The physics of premelted ice and its geophysical consequences *Rev. Mod. Phys.* **2006**, *78*, 695-741.

9 Wilen, L. A.; Wettlaufer, J. S.; Elbaum, M.; Schick, M. Dispersion-force effects in interfacial premelting of ice *Phys. Rev. B* **1995**, *52*, 12426-12433.

10 Lutzenkirchen, J.; Preocanin, T.; Kallay, N. A macroscopic water structure based model for describing charging phenomena at inert hydrophobic surfaces in aqueous electrolyte solutions *Phys. Chem. Chem. Phys.* **2008**, *10*, 4946-4955.

11 Wettlaufer, J. S. Impurity effects in the premelting of ice *Phys. Rev. Lett.* **1999**, *82*, 2516-2519.

12 Benatov, L.; Wettlaufer, J. S. Abrupt grain boundary melting in ice *Phys. Rev. E* **2004**, *70*, art. no. 061616.

13 Wettlaufer, J. S. Directional solidification of salt-water. Deep and shallow cells *Europhys. Lett.* **1992**, *19*, 337-342.